

# In-situ restructuring of Ni-based metal organic frameworks for photocatalytic CO<sub>2</sub> hydrogenation

Received: 29 June 2024

Accepted: 3 January 2025

Published online: 15 January 2025

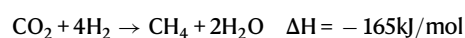
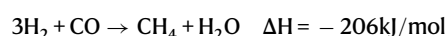
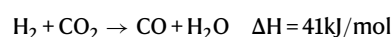
Check for updates

Abdelaziz Gouda <sup>1,2,3,7</sup> ✉, Karen Hannouche<sup>4,7</sup>, Abhinav Mohan<sup>2,3</sup>, Chengliang Mao <sup>1</sup>, Ehsan Nikbin<sup>5</sup>, Alexandre Carrière <sup>6</sup>, Jessica Ye <sup>1</sup>, Jane Y. Howe<sup>2,5</sup>, Mohini Sain <sup>2,3</sup> ✉, Mohamad Hmadeh <sup>1,4</sup> ✉ & Geoffrey A. Ozin <sup>1,2</sup> ✉

As the global quest for sustainable energy keeps rising, exploring novel efficient and practical photocatalysts remains a research and industrial urge. Particularly, metal organic frameworks were proven to contribute to various stages of the carbon cycle, from CO<sub>2</sub> capture to its conversion. Herein, we report the photo-methanation activity of three isostructural, nickel-based metal organic frameworks incorporating additional niobium, iron, and aluminum sites, having demonstrated exceptional CO<sub>2</sub> capture abilities from thin air in previous reports. The niobium version exhibits the highest performance, with a CO<sub>2</sub> to CH<sub>4</sub> conversion rate in the order of 750–7500 μmol\**g*<sub>catalyst</sub><sup>-1</sup>\**h*<sup>-1</sup> between 180 °C and 240 °C, achieving 97% selectivity under light irradiation and atmospheric pressure. The in-depth characterization of this framework before and after catalysis reveals the occurrence of an in-situ restructuring process, whereas active surface species are formed under photocatalytic conditions, thus providing comprehensive structure-performance correlations for the development of efficient CO<sub>2</sub> conversion photocatalysts.

Despite the global reliance on fossil fuels in most energy-demanding activities, the rapid depletion of these resources along with the severe threat they cause to the environment raises the urge to transition to greener alternatives. In fact, burning fossil fuels was reported to account for a cumulative of 1732 Pg emitted CO<sub>2</sub> thus causing a global warming of 0.78 °C<sup>1</sup>. Within this context, capturing CO<sub>2</sub> and converting it into solar fuels is a double-headed approach mitigating the excessive CO<sub>2</sub> emissions while producing value-added feed-stocks. One desirable example of such processes occurs through the Sabatier reaction, producing methane (CH<sub>4</sub>), one of the most energy-efficient fuels, and other organic molecules through the endothermic reverse water gas shift (RWGS) reaction combined with the exothermic CO

hydrogenation as follows<sup>2</sup>:



Although this reaction was traditionally performed under thermal conditions<sup>3,4</sup>, many reports proved that it could be, more appealingly, photo-induced<sup>5,6</sup> using a suitable semiconductor operating at mild

<sup>1</sup>Department of Chemistry, University of Toronto, Toronto, ON, Canada. <sup>2</sup>Department of Chemical Engineering and Applied Chemistry, University of Toronto, Toronto, ON, Canada. <sup>3</sup>Department of Mechanical and Industrial Engineering, University of Toronto, Toronto, ON, Canada. <sup>4</sup>Department of Chemistry, Faculty of Arts and Sciences, American University of Beirut, Beirut, Lebanon. <sup>5</sup>Department of Materials Science & Engineering, University of Toronto, Toronto, Canada. <sup>6</sup>Department of Engineering Physics, Polytechnique Montreal, Montreal, QC, Canada. <sup>7</sup>These authors contributed equally: Abdelaziz Gouda, Karen Hannouche. ✉ e-mail: [abdelaziz.gouda@utoronto.ca](mailto:abdelaziz.gouda@utoronto.ca); [m.sain@utoronto.ca](mailto:m.sain@utoronto.ca); [mohamad.hmadeh@aub.edu.lb](mailto:mohamad.hmadeh@aub.edu.lb); [g.ozin@utoronto.ca](mailto:g.ozin@utoronto.ca)

temperature and pressure. Over the years, numerous CO<sub>2</sub> methanation photocatalysts have been reported, including transition metal-based catalysts<sup>7,8</sup>, semiconductor metal oxides<sup>9,10</sup>, and perovskites<sup>11,12</sup>. However, it is worth noting that in most reports, desired efficiencies and selectivity were not attained using a single species<sup>13</sup>, a co-catalyst was rather needed or a host was used as a backbone for the active component<sup>14,15</sup>.

Metal-organic frameworks (MOFs), a class of hybrid, crystalline, and porous materials, were recently reported as good candidates for this host-guest synergy<sup>12</sup>. The large selection of metals and organic linkers from which MOFs can be constructed makes them particularly versatile, tunable, and efficient in a wide range of applications<sup>16–18</sup>. MOFs were capable of contributing to various components of the CO<sub>2</sub> cycle, from its capture to its conversion<sup>19</sup>. Owing to their ultra-porosity and high surface areas, MOFs can hold large quantities of gases, CO<sub>2</sub> in this case, in a confined space for extended periods<sup>20</sup>. Yaghi and co-workers reported one of the earliest records for CO<sub>2</sub> capture using MOF-2 with a CO<sub>2</sub> uptake of 3.2 mmol g<sup>-1</sup><sup>21</sup>. Ever since, many subfamilies of MOFs were reported to have exceptionally high CO<sub>2</sub> adsorption capacities including MIL<sup>22</sup>, PCN, and ZIFs<sup>23</sup> outperforming most of the state-of-the-art materials.

On the other hand, as MOFs are composed of positively charged metal nodes and negatively charged organic antennas, many charge separation pathways are possible within these frameworks, making them promising candidates for CO<sub>2</sub> photo-conversion<sup>24</sup>. However, to date, MOFs were mostly used as sacrificial precursors for the synthesis of active photo-methanation catalysts involving the destruction of the framework<sup>25,26</sup> or were reported to drive the Sabatier process thermally<sup>27,28</sup>. Only very few reports used MOFs as an active component in such photo-catalytic gas phase systems under milder conditions, including Cu<sub>2</sub>O decorated ZnO operating at 215 °C<sup>29</sup> and a titanium isophthalate MOF on which RuO<sub>x</sub> nanoparticles were deposited to yield 0.8 mmol (CH<sub>4</sub>)\*g<sub>catalyst</sub><sup>-1</sup> at 200 °C in 22 h<sup>30</sup>.

Herein, we investigate the CO<sub>2</sub> photo-methanation efficiencies of three isostructural MOFs based on Ni (II) and fluorinated pillars of niobium, aluminum, and iron, named respectively, NbOFFIVE-1-Ni (Ni-Nb-MOF), AlFFIVE-1-Ni (Ni-Al-MOF) and FeFFIVE-1-Ni (Ni-Fe-MOF). These MOFs are particularly known for their exceptional CO<sub>2</sub> adsorption, with NbOFFIVE-1-Ni having markedly demonstrated one of the best CO<sub>2</sub> capture abilities in confined spaces (at 400 ppm of CO<sub>2</sub> and 298 K) among physical adsorbents<sup>31</sup>. Since the photo-catalytic properties of these Ni-based MOFs were not investigated to date, we thought of making use of their very high affinity towards CO<sub>2</sub>, to drive the Sabatier process under mild conditions. The Ni-Nb-MOF candidate performs best, demonstrating a CO<sub>2</sub> conversion rate of 750 μmol\* g<sub>catalyst</sub><sup>-1</sup>\*h<sup>-1</sup> with a remarkable selectivity towards CH<sub>4</sub> formation (97%) at 180 °C and atmospheric pressure. More interestingly, this enhanced photo-activity is hypothesized to occur because of the in-situ formation of Nb<sub>2</sub>CT<sub>x</sub>/Nb<sub>2</sub>O<sub>5</sub> heterojunctions dispersed on the surface of the framework which retains its crystallinity. The formation of these highly active species is thought to occur via MOF surface restructuring within the induction time needed (around 75 min) for methane production to rise. A similar observation was reported when intentionally heating Ni-MOF-74 to partially decompose the framework and generate nickel nanoparticles dispersed on the pyrolyzed MOF backbone (Ni@MOF-74)<sup>32</sup>. The isostructural MOFs are characterized before and after photocatalytic testing and a thorough understanding of the enhanced activity of NbOFFIVE-1-Ni in comparison with its Al and Fe counterparts is established. <sup>13</sup>C isotope labeling experiments ensure that the evolved CH<sub>4</sub> is derived from CO<sub>2</sub>, thus proving the facile in-situ synthesis and photo-methanation efficiency of such active MOF composites.

## Results

### Structural analysis of the synthesized MOFs

In this study, three catalytic MOF candidates were synthesized, all sharing a similar topology in which Ni<sup>2+</sup> cations are connected to the pyrazine linkers in a square grid motif. These formed entities are cross-linked to the inorganic (NbOF<sub>3</sub>)<sup>2-</sup> pillar for Ni-Nb-MOF and [MF<sub>5</sub>(H<sub>2</sub>O)]<sup>2-</sup> (M = Al<sup>3+</sup> or Fe<sup>3+</sup>) pillars in the case of Ni-Al-MOF and Ni-Fe-MOF (Fig. 1a). PXRD patterns of the synthesized MOFs are shown in Fig. 1b and are in agreement with the reported ones<sup>31,33</sup> and their rectangular morphologies were visualized by TEM and SEM and are shown in Figs. 1c–e and Supplementary Fig. 1 respectively. The particle size distribution of the three MOFs was estimated from their corresponding TEM images (>20 particles from 5 different TEM images for each) and the results are shown in Supplementary Fig. 2. As demonstrated by the TGA curves (Supplementary Fig. 3), both Ni-Al MOF and Ni-Fe MOF are subjected to dehydration at temperatures near 100 °C, with Ni-Fe-MOF being the least thermally stable among the three studied structures. This thermal stability will greatly affect the catalytic performance and recyclability throughout the photo-methanation reaction as will be discussed in the upcoming sections.

### Spectral analysis and electronic structure elucidation

In order to gain a deeper understanding of the optical properties of the synthesized MOFs, UV-Vis diffuse reflectance spectra were recorded for the three studied frameworks (Supplementary Fig. 4). The three isostructural MOFs present some common spectral features mainly around 350 nm and 700 nm. The nearly overlapping peaks at 350 nm can be attributed to the electronic transitions occurring within the conjugated pyrazine π system while the common peak at around 700 nm is a characteristic feature of octahedrally coordinated nickel (II) complexes<sup>34</sup>. Moreover, cyclic voltammetry (CV) measurements were employed to compare the charge transfer properties of the frameworks (Supplementary Fig. 5). The three MOF structures share the same characteristics as their pyrazine linker (–0.24 V and –0.80 V vs Ag/AgCl) with Ni-Nb-MOF and Ni-Fe-MOF having the largest voltametric current. Similarly, these two frameworks exhibit a low total resistance in the high-frequency region in Nyquist plots as compared to Ni-Al-MOF and the pyrazine linker. Both CV and electrochemical impedance spectra (EIS) results suggest a higher charge carrier separation and electron transfer efficiency in Ni-Fe-MOF and Ni-Nb-MOF.

### Assessment of the photo-catalytic performance of the three Ni-based MOFs

The photo-methanation tests were performed in a flow mode at ambient pressure and mild temperature (180 °C) compared to what was previously reported<sup>35,36</sup>. LED light, with an emission spectrum shown in Supplementary Fig. 6, was used as a source of irradiation with a light intensity of 4.6 W/cm<sup>2</sup> in all optimized tests. The variation of the LED light irradiance with respect to the light composition is tabulated in Supplementary Table 1. The initial catalytic screening was performed using a (1:1) (CO<sub>2</sub>:H<sub>2</sub>) gas mixture for the three investigated MOFs. As can be seen in Fig. 2, Ni-Nb-MOF and Ni-Fe-MOF demonstrated high conversions and selectivity towards methane and CO respectively, while Ni-Al-MOF did not show any catalytic activity. Both performant MOFs operated well under a continuous flow of reactants and demonstrated a steady catalytic activity starting from the second hour of testing. The role of light in the catalytic reaction itself was demonstrated by switching the LED source off for 100 min after both MOFs had reached maximum conversion rates, and an immediate drop of CH<sub>4</sub> and CO rates was observed (Supplementary Fig. 7). Switching the light back on restores the products formation rate immediately, indicating that the CO<sub>2</sub> hydrogenation occurring on the surface of Ni-Nb and Ni-Fe MOFs is driven by light.

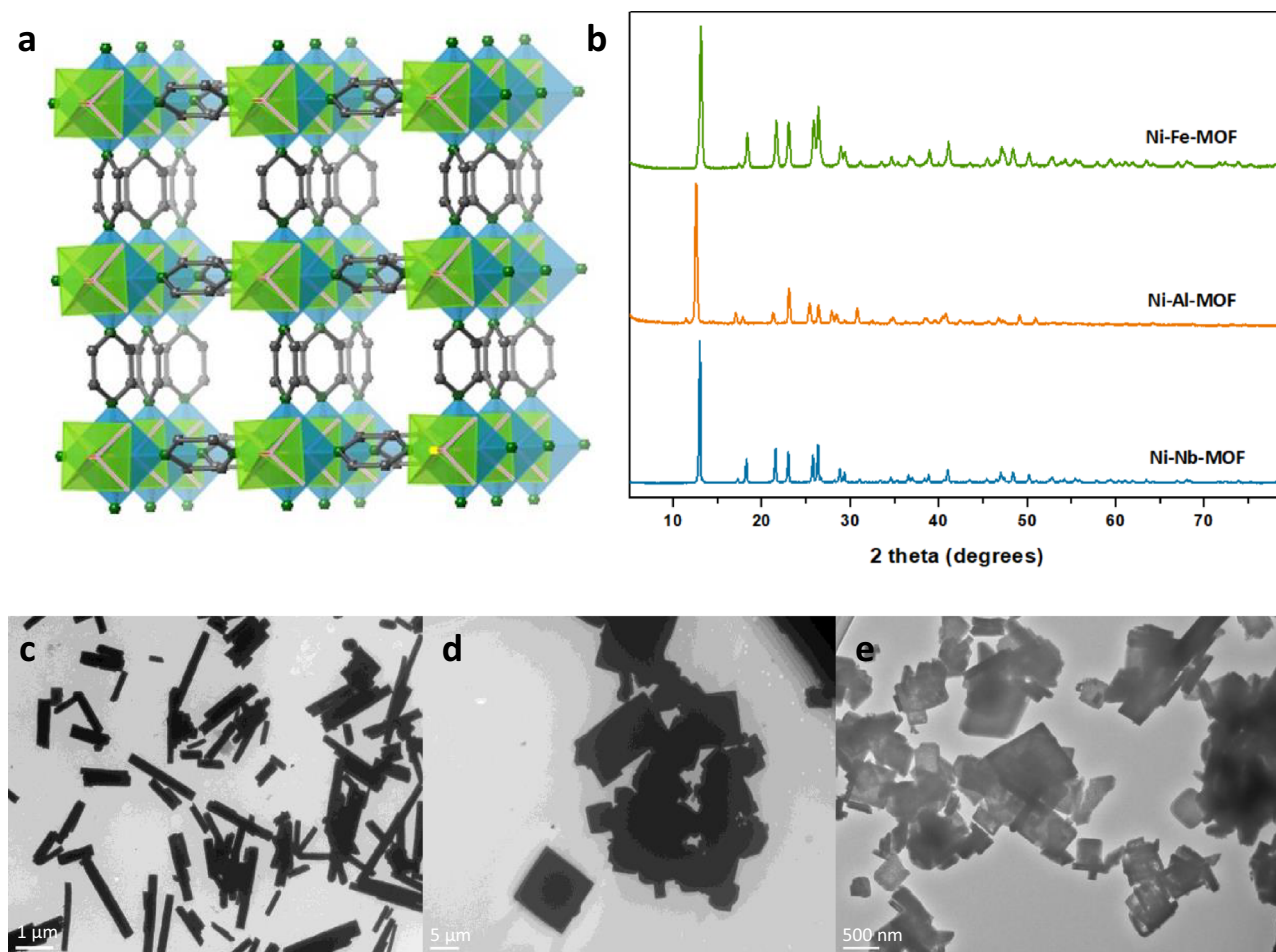


**Fig. 1 | Crystal structure and characterization of the three as-synthesized isostructural MOFs.** **a** Schematic illustration of Ni-based MOF structures (Ni centers in blue, Nb, Al, and Fe pillars in light green, N atoms in dark green, and C atoms

in grey). **b** PXRD patterns of the three synthesized MOFs (Ni-Nb-MOF in blue, Ni-Al-MOF in orange, and Ni-Fe-MOF in green). TEM images of **c** Ni-Nb-MOF (scale bar = 1  $\mu\text{m}$ ), **d** Ni-Al-MOF (scale bar = 5  $\mu\text{m}$ ), and **e** Ni-Fe-MOF (scale bar = 500 nm).

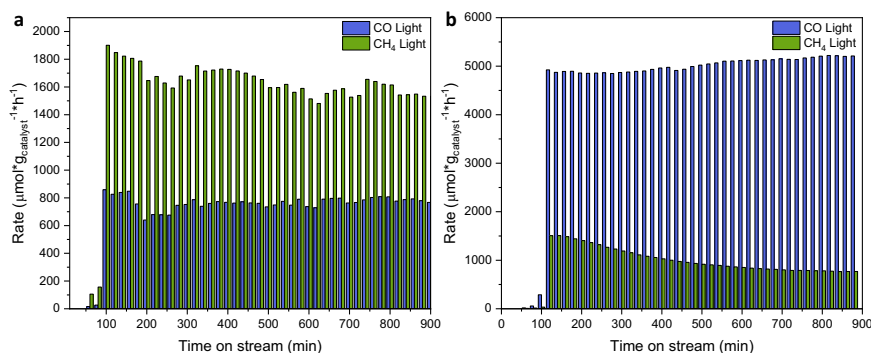


**Fig. 2 | Flow-mode photocatalytic testing of Ni-Nb-MOF and Ni-Fe-MOF using (1:1) (CO<sub>2</sub>: H<sub>2</sub>) and 4.6 W/cm<sup>2</sup> LED light.** Comparison between the photocatalytic rates of CH<sub>4</sub> (green bars) and CO (blue bars) formation using **a** Ni-Nb-MOF and **b** Ni-

Fe-MOF over 900 mins with continuous (1:1) (CO<sub>2</sub>: H<sub>2</sub>) flow and 4.6 W/cm<sup>2</sup> LED light irradiation.

In order to verify the source of the obtained products for both performant MOFs, <sup>13</sup>C isotope labeling experiments were conducted and the fractions of <sup>13</sup>CH<sub>4</sub> and <sup>13</sup>CO produced were calculated at three reaction times:  $t = 3, 15,$  and  $27$  h using GC-MS. Results present in Fig. 3 confirm that the methane and carbon monoxide produced using Ni-Nb-MOF clearly originate from CO<sub>2</sub>, while lower <sup>13</sup>CH<sub>4</sub> and <sup>13</sup>CO ratios were obtained with Ni-Fe-MOF as a catalyst. Particularly, it is known that the standard <sup>12</sup>CH<sub>4</sub> and <sup>13</sup>CH<sub>4</sub> mass patterns involve  $m/z = 12, 13, 14, 15, 16, 17,$  and  $m/z = 13, 14, 15, 16, 17, 18,$  respectively, with their

relative intensity ratios being 380: 1069: 2042: 8879: 9999: 164. Therefore, the intensity ratio between  $m/z = 17$  and  $m/z = 16$  can be used to quantify the relative molar fraction of <sup>12</sup>CH<sub>4</sub> and <sup>13</sup>CH<sub>4</sub> in their mixture via Eq. (1).

$$^{13}\text{CH}_4\% = \frac{I_{17} - 0.0164}{1.13 - 0.0164} \times 100\% \quad (1)$$

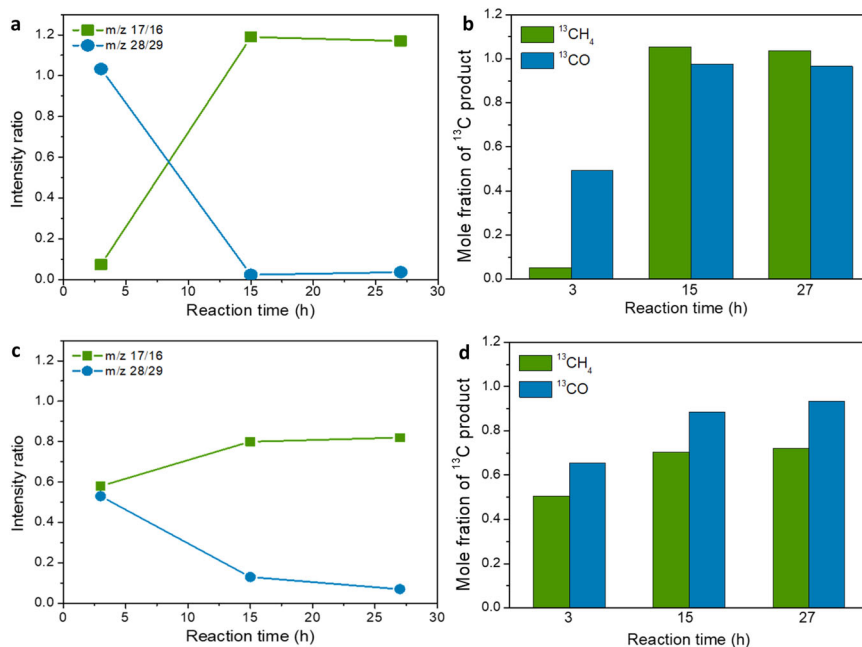


**Fig. 3** |  $^{13}\text{CO}_2$  isotope labeling experiments for Ni-Nb-MOF and Ni-Fe-MOF quantified by GC-MS. **a** Mass over charge ( $m/z$ ) ratios of  $^{13}\text{CH}_4/^{12}\text{CH}_4$  ( $m/z$  17/16, green line) and  $^{12}\text{CO}/^{13}\text{CO}$  ( $m/z$  28/29, blue line) formed when using Ni-Nb-MOF as a catalyst. **b** Mole fractions of  $^{13}\text{CH}_4$  (green bars) and  $^{13}\text{CO}$  (blue bars) produced when using  $^{13}\text{CO}_2$  as a reactant and Ni-Nb-MOF as a catalyst. Ratios calculated at 3 different reaction times (3, 15, and 27 h) demonstrate that nearly the total amount of both products originated from  $\text{CO}_2$ . **c** Mass over charge ( $m/z$ ) ratios of  $^{13}\text{CH}_4/^{12}\text{CH}_4$

( $m/z$  17/16, green line) and  $^{12}\text{CO}/^{13}\text{CO}$  ( $m/z$  28/29, blue line) formed when using Ni-Fe-MOF as a catalyst. **d** Mole fractions of  $^{13}\text{CH}_4$  (green bars) and  $^{13}\text{CO}$  (blue bars) produced when using  $^{13}\text{CO}_2$  as a reactant and Ni-Fe-MOF as a catalyst. All ratios calculated at 3 different reaction times (3, 15, and 27 h) are less than 1, indicating that a considerable amount of products formed on the surface of Ni-Fe-MOF originates from a carbon source other than  $\text{CO}_2$ . All photocatalytic reactions were conducted at 180 °C, using (1:1) ( $\text{CO}_2$ :  $\text{H}_2$ ) and 4.6  $\text{W}/\text{cm}^2$  LED light.

where  $I_{17}$  and  $I_{16}$  are the intensities of  $m/z = 17$  and 16, respectively, 1.13 and 0.0164 are  $I_{17}/I_{16}$  intensity ratios of standard  $^{12}\text{CH}_4$  and  $^{13}\text{CH}_4$ , respectively.

Similarly,  $I_{28}/I_{29}$  ratios of standard  $^{12}\text{CO}$  and  $^{13}\text{CO}$  mass patterns are 833.25 and 0, respectively, which can be used to calculate the relative molar fraction of  $^{12}\text{CO}$  and  $^{13}\text{CO}$  in their mixture via Eq. (2).

$$^{13}\text{CO}\% = \frac{1}{\frac{I_{28}}{I_{29}} + 1} \times 100\% \quad (2)$$

Moreover, while Ni-Nb-MOF retained its crystallinity throughout the catalytic reaction, Ni-Fe-MOF was completely destroyed as evidenced in the recorded PXRD patterns and TEM images of the samples after reaction, as discussed in the following section. Thus, tracing back the source of the products formed in the case of Ni-Fe-MOF, the organic backbone of the destroyed framework might account for the isotopically unlabeled methane and carbon monoxide produced. This framework degradation was in line with the low thermal stability of Ni-Fe-MOF (below 200 °C) making it hard to withstand the mild reaction temperature used. Nevertheless, the catalytic activity of this unstable MOF can be attributed to the formation of active Fe and Ni sites on the carbon matrix that originates from the decomposed MOF backbone. It is worth noting here that iron-based catalysts are usually reported to selectively favor the formation of CO in the Sabatier process<sup>37,38</sup>, which correlates well with the shifted selectivity of Ni-Fe-MOF studied in this work. The nature of these active sites will be validated by XPS and HRTEM characterization after methanation, as detailed in the subsequent section.

Furthermore, as an attempt to rationalize the shift in selectivity between Ni-Nb-MOF and Ni-Fe-MOF, time-dependent in-situ diffuse reflectance infrared Fourier transform spectroscopy (DRIFTS) was performed after restructuring to identify the different intermediates formed on the surface of both MOFs as the products start to be

released. A comparison between the DRIFTS spectra of Ni-Nb and Ni-Fe MOFs at a fixed timing (Supplementary Fig. 8) shows the presence of common peaks between the two MOFs, notably those pertaining to adsorbed  $\text{CO}_2$  (1230–1270  $\text{cm}^{-1}$ ), coordinated CO (1770–2000  $\text{cm}^{-1}$ ) and monodentate and polydentate surface carbonates (1300–1700  $\text{cm}^{-1}$ ). A slight shift towards lower wavenumbers is observed for Ni-Nb-MOF in comparison with Ni-Fe-MOF, especially in the coordinated CO region, indicating the presence of weaker C–O bonds hence stronger M–C bonds<sup>39,40</sup> on the surface of Ni-Nb-MOF. This observation aligns well with the fact that intermediates with a greater binding strength can accept additional electrons and protons on the catalyst's surface to form highly reduced products<sup>41</sup>. In line with this rationale, CO is an intermediate which is strongly bound and subsequently reduced to methane by Ni-Nb-MOF, while being a released product in the case of Ni-Fe-MOF. Moreover, distinctive peaks were identified in the case of Ni-Nb-MOF, with characteristic formate peaks appearing at 1390  $\text{cm}^{-1}$  and 1585  $\text{cm}^{-1}$ ,  $-\text{CH}_3$  asymmetric bend at 1478  $\text{cm}^{-1}$ , and a characteristic methanol band at 1005  $\text{cm}^{-1}$ . The formation of these intermediates was tracked by time-dependent in-situ DRIFTS (Supplementary Fig. 9a) performed after restructuring, for 24 mins, with a spectrum recorded every 2 mins. The increase in formate,  $-\text{CH}_3$ , and CO peak intensities with respect to  $t = 0$  highlights their role as key intermediates for the Sabatier process<sup>42–44</sup>, and can lead to methane production via two routes, illustrated in Supplementary Fig. 10a. The formate pathway also called associative methanation occurs when adsorbed  $\text{CO}_2$  is converted to formate, and subsequently to methane. On the other hand, the CO pathway, also called dissociative methanation, involves the dissociation of  $\text{CO}_2$  into  $^*\text{CO}$  and  $^*\text{O}$  followed by the dissociation of  $^*\text{CO}$  into  $^*\text{C}$  which is then hydrogenated to  $\text{CH}_4$ <sup>45</sup>. Both routes release two water molecules in total, and both can possibly occur in the case of Ni-Nb-MOF. The absence of these characteristic bands along with the appearance of a strong carboxylate peak at 1545  $\text{cm}^{-1}$ , which intensity increases with time, in the case of Ni-Fe-MOF (Supplementary Fig. 9b)

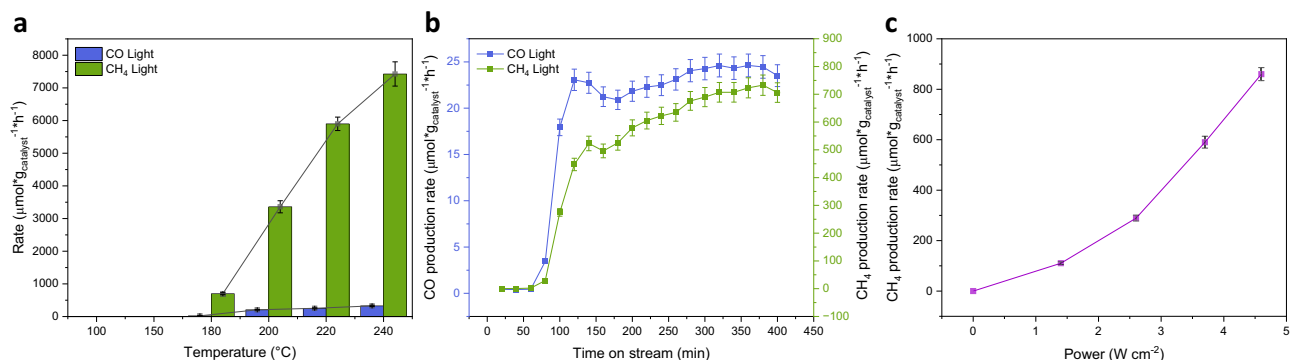


**Fig. 4 | Photocatalytic activity and selectivity of Ni-Nb-MOF under optimized conditions.** **a** Photocatalytic performance of Ni-Nb-MOF at different reaction temperatures, ranging between a threshold temperature of 180 °C and 240 °C. CH<sub>4</sub> formation rate is represented by green bars while blue bars are used for CO formation rate. **b** CH<sub>4</sub> (green line and symbol) and CO (blue line and symbol) production over time. An induction time of 75 mins is observed beyond which both

products start to form. **c** CH<sub>4</sub> production rates at different light intensities, giving an exponential profile represented by purple line and symbols. All photocatalytic reactions were conducted using (1:4) (CO<sub>2</sub>:H<sub>2</sub>), 4.6 W/cm<sup>2</sup> LED light intensity and Ni-Nb-MOF as a catalyst. Error bars represent the standard deviation of the averaged data recorded in triplicates.

explains the shift in selectivity towards CO formation<sup>46</sup> through the RWGS reaction, suggesting an associative pathway (Supplementary Fig. 10b) in which adsorbed CO<sub>2</sub> is hydrogenated to form a COOH\* intermediate to subsequently form CO and one water molecule.

#### Assessment of the photo-methanation activity and selectivity of Ni-Nb-MOF

Ni-Nb-MOF was selected as the most active, methane-selective, and stable candidate for the studied Sabatier process, and several reaction conditions were refined to optimize its performance. In fact, for selectivity enhancement, (1:4) ratios of (CO<sub>2</sub>: H<sub>2</sub>) were used instead of (1:1) ratios, and the reaction was performed at several temperatures ranging from 23 to 240 °C. As can be seen in Fig. 4a, no catalytic conversion was detected below 180 °C and the CH<sub>4</sub> formation rate increases linearly with temperature reaching 7500  $\mu\text{mol} \cdot \text{g}_{\text{catalyst}}^{-1} \cdot \text{h}^{-1}$  at 240 °C. Nevertheless, for this process to be scalable to an industrial level, mild reaction temperatures are favored, hence further tests were performed at 180 °C, the lowest applicable temperature in this case.

When tested at 180 °C, over a time stream of 400 mins, Ni-Nb-MOF seems to require an induction time of 75 mins after which the conversion rate increases rapidly while being 33 times more selective towards methane production attaining a plateau of 750  $\mu\text{mol} \cdot \text{g}_{\text{catalyst}}^{-1} \cdot \text{h}^{-1}$  (Fig. 4b). Neither CH<sub>4</sub> nor CO are produced in the absence of CO<sub>2</sub> or light (Supplementary Figs. 11–12). These observations suggest that the actual active catalytic species derived from Ni-Nb-MOF were formed upon light illumination, within the reaction's induction time, a transformation that is thoroughly investigated in the upcoming sections. Moreover, a control test was performed in which Ni-Nb-MOF was irradiated under CO<sub>2</sub> only throughout the induction time. No subsequent formation of CH<sub>4</sub> nor CO was detected, indicating the role of the reductive atmosphere in the formation of the catalyst's active state.

Mechanistically, CO<sub>2</sub> photo-methanation can occur via photochemical and/or photothermal pathways. While the former involves charge carriers' separation upon light irradiation, the second transforms light into heat to drive the reaction forward<sup>47</sup>. As an attempt to determine which of these two pathways is dominant in the case of Ni-Nb-MOF, the surface temperature of Ni-Nb-MOF was measured to be 120 °C using a forward-looking infrared camera (FLIR) under the same reaction conditions, but without heating and under a light intensity of 4.6 Wcm<sup>-2</sup> as shown in Supplementary Fig. 13. Additionally, CH<sub>4</sub> production rate was measured at different light intensities (at 180 °C, using (1:4) (CO<sub>2</sub>: H<sub>2</sub>) and Ni-Nb-MOF as a catalyst) (Fig. 4c), and the rate

increase turned out to be exponential, indicating the dominance of a photothermal methanation.

Table 1 compares the performance of Ni-Nb-MOF with respect to the latest MOF-based state-of-the-art catalysts in CO<sub>2</sub> photo-methanation. It is worth noting here that these rates should also be correlated to the reaction conditions used for each catalytic system (temperature, pressure, and light irradiation), thus placing Ni-Nb-MOF among the few examples operating under moderate light intensity and mild conditions, with a CH<sub>4</sub> conversion of 7.5  $\text{mmol} \cdot \text{g}_{\text{catalyst}}^{-1} \cdot \text{h}^{-1}$  at 240 °C. Other MOF-derived catalytic systems demonstrated exceptionally high conversion rates<sup>36,48</sup>, however, they involved the consumption of the framework throughout the light-driven process, contrarily to Ni-Nb-MOF which retained its crystallinity under the reaction conditions used.

#### Investigation of the in-situ restructuring process through post-catalysis characterization

In order to understand the enhanced activity and selectivity of Ni-Nb-MOF compared to its Al and Fe counterparts, post-methanation characterization was performed starting from transmission electron microscopy (TEM) and scanning transmission electron microscopy (STEM) imaging. In fact, Ni-Nb-MOF morphology was conserved while surprisingly being speckled with lower contrast sites indicating the formation of well-dispersed particles within the framework as shown in the annular dark-field (ADF) STEM image (Fig. 5a and Supplementary Fig. 14a). Such surface alterations were not observed when performing the reaction thermally at 300 °C (Ni-Nb-MOF surface temperature (120 °C) + 180 °C), without light irradiation as shown in Supplementary Fig. 15. As for Ni-Fe MOF, the well-defined dimensions of the crystal are substituted by the homogeneous distribution of particles (Fig. 5c and Supplementary Fig. 14c), suspected to be active Ni and Fe species. On the other hand, Ni-Al-MOF TEM and STEM images do not show formation of any of these nanoparticles (Fig. 5b and Supplementary Fig. 14b), which was hypothesized to be the reason behind the poor catalytic activity of this MOF. The size distribution of the surface particles depicted in the STEM images of Ni-Nb-MOF and Ni-Fe-MOF in Supplementary Fig. 14a and Supplementary Fig. 14c respectively, was measured as shown in Supplementary Fig. 16 to gain some insights about the size range of these surface aggregates which will be subsequently imaged under high-resolution transmission electron microscopy (HRTEM).

Atomic force microscopy (AFM) was performed to examine the surface features of spent Ni-Nb and Ni-Fe MOFs after sonication in

**Table 1 | Summary of MOF-based state-of-the-art materials reported as selective photocatalysts for CO<sub>2</sub> conversion to CH<sub>4</sub>**

	Conditions	CH <sub>4</sub> Conversion Rates (mmol g <sub>catalyst</sub> <sup>-1</sup> h <sup>-1</sup> )	CH <sub>4</sub> Selectivity	Ref
1%Cu <sub>2</sub> O@MOF(Zn)-1	<ul style="list-style-type: none"> <li>■ 0.2236 W/cm<sup>2</sup> (300 W Xe lamp)</li> <li>■ T = 215 °C</li> <li>■ P = 1.3 bar</li> <li>■ (H<sub>2</sub>:CO<sub>2</sub>): (4:1)</li> </ul>	0.0019	No other products detected.	29
MIP-208@RuO <sub>x</sub>	<ul style="list-style-type: none"> <li>■ 0.135 W/cm<sup>2</sup></li> <li>■ T = 200 °C</li> <li>■ P = 1.3 bar</li> <li>■ (H<sub>2</sub>:CO<sub>2</sub>): (4:1)</li> </ul>	0.036	No other products detected.	30
1%RuO <sub>x</sub> @UiO-66(Zr/Ce/Ti)	<ul style="list-style-type: none"> <li>■ 150 W Hg-Xe lamp</li> <li>■ T = 200 °C</li> <li>■ P = 1.3 bar</li> <li>■ (H<sub>2</sub>:CO<sub>2</sub>): (4:1)</li> </ul>	0.13	100%	72
1%RuO <sub>x</sub> @UiO-66(Zr/Ti)-NO <sub>2</sub>	<ul style="list-style-type: none"> <li>■ 0.2 W/cm<sup>2</sup></li> <li>■ T = 200 °C</li> <li>■ P = 1.5 bar</li> <li>■ (H<sub>2</sub>:CO<sub>2</sub>): (4:1)</li> </ul>	0.23	>99%	73
10%RuO <sub>x</sub> @MIL-125(Ti)-NH <sub>2</sub>	<ul style="list-style-type: none"> <li>■ 150 W Hg-Xe lamp</li> <li>■ T = 200 °C</li> <li>■ P = 1.3 bar</li> <li>■ (H<sub>2</sub>:CO<sub>2</sub>): (4:1)</li> </ul>	0.84	No other products detected.	35
<b>In situ restructured NbOFFIVE-1-Ni</b>	<ul style="list-style-type: none"> <li>■ <b>4.6 W/cm<sup>2</sup> (LED light source).</b></li> <li>■ <b>T = 180 °C</b></li> <li>■ <b>P = 1 atm</b></li> <li>■ <b>(H<sub>2</sub>:CO<sub>2</sub>): (4:1)</b></li> </ul>	<b>0.75</b>	<b>97%</b>	<b>This work</b>
<b>In situ restructured NbOFFIVE-1-Ni</b>	<ul style="list-style-type: none"> <li>■ <b>4.6 W/cm<sup>2</sup> (LED light source).</b></li> <li>■ <b>T = 240 °C</b></li> <li>■ <b>P = 1 atm</b></li> <li>■ <b>(H<sub>2</sub>:CO<sub>2</sub>): (4:1)</b></li> </ul>	<b>7.5</b>	<b>97%</b>	<b>This work</b>

<sup>a</sup>Entries in bold represent the conditions and results of this work.

isopropanol and the results are shown in Supplementary Figs. 17, 18. While the Ni-Nb-MOF sample after catalysis shows thin, plate-like features of few nm in thickness, big aggregates are visualized in the Ni-Fe sample after catalysis. Zooming into some features of the latter, the stacked particles have an average thickness of 110 nm, with a much higher surface roughness that may be due to the non-homogeneity of the destructed MOF backbone and the active species formed under the reaction's conditions.

As a comparison of the metal composition of Ni-Nb and Ni-Fe MOFs before and after catalysis, inductively coupled plasma optical emission spectroscopy (ICP-OES) analysis was conducted on fresh and spent MOF samples and the results are shown in Supplementary Fig. 19. While the total metal composition remains the same in Ni-Nb-MOF before and after catalysis, the total metal percentage increases from 31 to 39% in the case of Ni-Fe-MOF, indicating the partial loss of the catalyst's organic component. The relative Ni: Nb and Ni: Fe percentages were calculated from ICP-OES results (Supplementary Table 2) and compared to the percentages estimated from scanning electron microscopy-energy dispersive X-ray (SEM-EDX) (Supplementary Table 3). While percentage trends are comparable in both techniques, Nb % in the spent Ni-Nb-MOF calculated from SEM-EDX is high (59% as compared to 44% from ICP-OES). In fact, while ICP-OES accurately determines the bulk composition of each material, SEM-EDX gives an estimation of the metal content on the material's surface, indicating that Nb is more exposed than Ni on the surface of Ni-Nb-MOF. The EDS maps of the three MOF candidates after reaction (Supplementary Figs. 20–22) show the elemental distribution on the frameworks' surfaces.

While PXRD patterns of Ni-Nb-MOF and Ni-Al-MOF before and after methanation remain unchanged, those of Ni-Fe-MOF indicate the complete loss of crystallinity (Fig. 5d–f). It is worthy to note that no additional peaks, that would be attributed to the surface species formed upon restructuring, appeared in the patterns of Ni-Nb and Ni-Fe MOFs after methanation. This may be due to the undetectable

concentration of these active species on the Ni-Nb-MOF backbone on one hand and the carbon matrix of the consumed Ni-Fe-MOF on the other hand. Additionally, DRS spectra of the three spent MOF catalysts were recorded (Supplementary Figs. 23, 24) and the band gap of each species before and after methanation was estimated from the corresponding Tauc plots (Supplementary Figs. 25–27). While the band gap of Ni-Al-MOF stayed virtually the same throughout the reaction (-3.1 eV), the bandgaps of the Nb and Fe-based MOFs were narrowed, further confirming the formation of optically active species throughout the reaction.

FTIR-coupled TGA was conducted on both highly performing candidates to depict whether these surface species are formed upon thermal destruction or light irradiation. FTIR spectra were recorded for the released species at 180 °C (the tests' temperature), 300 °C (the total surface temperature of both MOFs as determined by FLIR camera), and temperatures relevant to major decomposition steps in the TG profile of both MOFs. As shown in Supplementary Fig. 28, Ni-Nb-MOF is stable at 180 and 300 °C, with no detectable released products at the test's temperature indicating that no thermal decomposition is occurring. On the other hand, Ni-Fe-MOF is subjected to a loss of hydroxyl groups at low temperatures, which can be attributed to the dehydration of its [FeF<sub>5</sub>(H<sub>2</sub>O)]<sup>2-</sup> pillar. At 300 °C, the actual surface temperature of the catalyst during testing, decomposition products are detected matching some FTIR vibrations of pyrazine. In fact, the observed bands at 785, 1026, 1418 and 3070 cm<sup>-1</sup> can be attributed to  $\nu(\text{CH})$ ,  $\delta_{\text{ring}}$ ,  $\nu_{\text{ring}}$  and  $\nu(\text{C-H})$  respectively<sup>49,50</sup>, further confirming the destruction of the framework and the loss of some of its organic component. A similar IR spectrum was observed beyond 400 °C in the case of Ni-Nb-MOF (Supplementary Fig. 28a) in alignment with the thermal stability trend of the isostructural MOFs.

In an attempt to identify the active species formed on the surface of Ni-Nb-MOF and upon decomposition of Ni-Fe-MOF in comparison to Ni-Al-MOF, the oxidation state of the major elements found in these structures was tracked by XPS measurements performed on fresh and

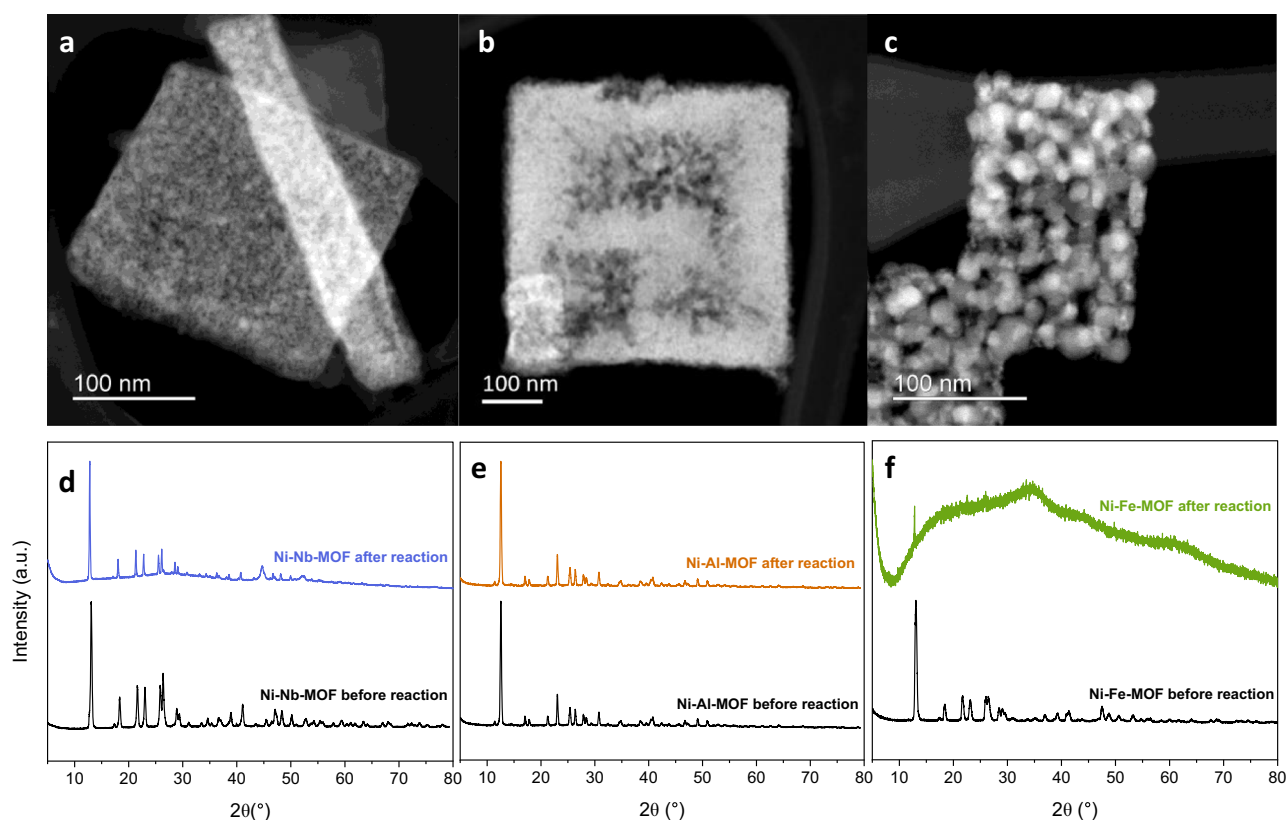


**Fig. 5 | Post-reaction morphological and structural characterization of the three isostructural MOFs.** ADF-STEM images of **a** Ni-Nb-MOF, **b** Ni-Al-MOF, and **c** Ni-Fe-MOF after the photocatalytic reaction (scale bar = 100 nm). Comparison between PXRD patterns of the three MOFs before and after catalysis. **d** PXRD

patterns of Ni-Nb-MOF (black line before reaction, blue line after reaction), **e** PXRD patterns of Ni-Al-MOF (black line before reaction, orange line after reaction), and **f** PXRD patterns of Ni-Fe-MOF (black line before reaction, green line after reaction).

spent samples of the three MOFs. While the binding energies of C, N, O, F, and Ni stayed virtually the same in the Ni-Nb-MOF sample (Supplementary Figs. 29–32), the Nb  $3d_{3/2}$  and Nb  $3d_{5/2}$  peaks demonstrate a shift towards lower binding energies as compared to the fresh sample (from 211 eV to 210 eV and from 208 eV to 207 eV respectively) (Fig. 6a, b). This observation implies that Nb is reduced from a fully oxidized form in the parent structure (Nb (V)) to a lower oxidation state in the restructured catalyst. Similarly, for Ni-Fe-MOF, only Fe demonstrated a change in binding energy throughout the reaction with the Fe  $2p$  peaks being shifted from 714 eV to 711 eV and 727.5 eV to 725 eV respectively (Fig. 6c, d), suggesting a decrease in Fe oxidation state from (+III) to (+II). It is also worth noting that the N  $1s$  peak disappeared from the full XPS spectrum of Ni-Fe-MOF (Supplementary Figs. 38, 39) which is in alignment with the loss of pyrazine demonstrated by TGA-FTIR, and further indicates that the species formed upon the framework's destruction do not contain nitrogen. The full XPS spectra of Ni-Nb, Ni-Al, and Ni-Fe MOF before and after the catalytic reaction are presented in Supplementary Figs. 29–41.

In order to confirm the nature of these reduced niobium and iron species, d-spacings were calculated from HRTEM images of the speckled domains present on the surface of the spent samples after catalysis. The selected area electron diffraction (SAED) of Ni-Nb-MOF after reaction (Fig. 7a) further confirms the retained crystallinity of the MOF structure. The SAED pattern shows the diffraction pattern from the  $[0\ 0\ 1]$  zone axis of the crystal. The measured d-spacing of 7.0 Å for the  $(1\ 1\ 0)$  spot matches well with the crystal structure of the framework<sup>31</sup>. Moreover, as can be seen in the HRTEM images of Fig. 7b, c spacings of 1.88 Å and 2.08 Å can be ascribed, respectively, to the  $(102)$  and  $(421)$  planes of  $Nb_2CT_x$ , typically known as Nb-based

MXenes<sup>51,52</sup>. MXenes were first reported in 2011<sup>53</sup> as 2D early transition metal-based carbides and carbonitrides having  $M_{n+1}X_nT_x$  as general formula<sup>54</sup> (where M can be Nb, Ti, V or Zr, X is C and/or N and T is a terminal group such as -OH, -O and/or -F). This fast-growing family of materials was proven to be potent in many optical and electrical applications, notably in photocatalysis, where it promotes an efficient charge separation while allowing for better contact between the catalyst and the reactants<sup>55</sup>. More interestingly, MXenes can be partially or totally oxidized into their corresponding metal oxides upon exposure to oxygen-containing species such as  $CO_2$ <sup>56</sup>. Hence, the calculated d spacings that matched with  $Nb_2CT_x$  planes along with the additional recurrent 3.14 Å value which is typically attributed to  $Nb_2O_5$  (100) diffraction plane<sup>57</sup>, are indicative of the in-situ formation of  $Nb_2CT_x$  MXenes on the surface of the framework, and their partial oxidation to  $Nb_2O_5$  to form a photocatalytically active heterojunction.  $Nb_2O_5/Nb_2CT_x$  heterojunctions were in fact reported to catalyze various light-driven reactions<sup>56</sup>. This hypothesis is in accordance with the thin sheets observed in the Ni-Nb sample after reaction by AFM (Supplementary Fig. 17) and the increase in Nb% on the surface of spent Ni-Nb-MOF demonstrated by SEM-EDX (Supplementary Table 3). In addition to that, the DRS spectrum of Ni-Nb-MOF after reaction (Supplementary Fig. 24) shows the disappearance of reflectance peaks between 1300 and 2000 nm, that are usually attributed to -OH overtones and combination bands of water<sup>58,59</sup>, a product that is released throughout the methanation reaction. While no surface species were identified from this DRS comparison, the absence of these peaks in the NIR region is in accordance with the reported spectrum of  $Nb_2CT_x$ <sup>60</sup>. This is further confirmed by XPS results, since in the abundant  $Nb_2CT_x$  species, Nb has a (+IV) oxidation state. It is worth noting here that the synthesis

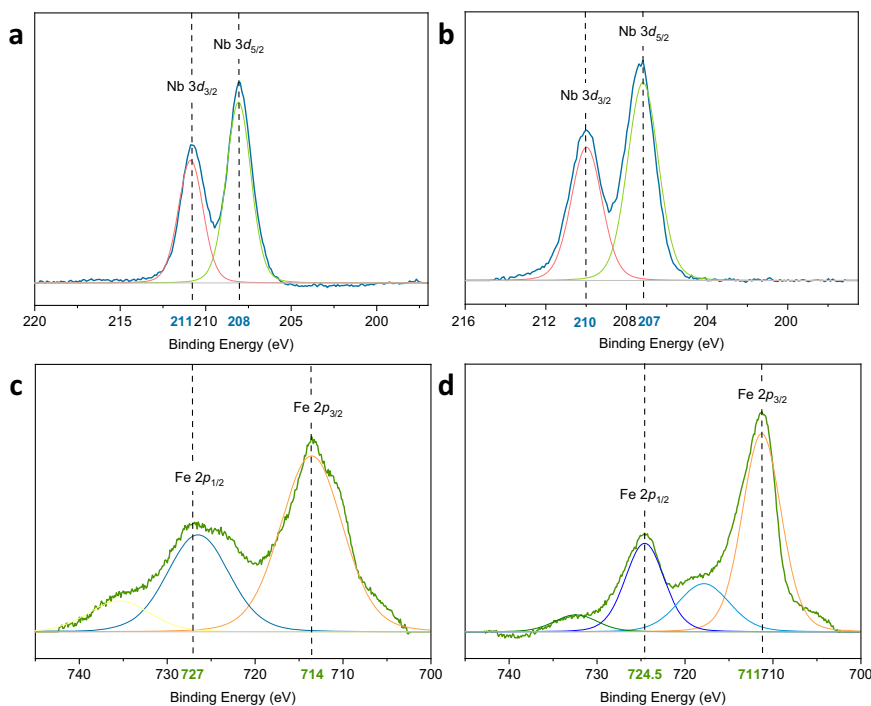


**Fig. 6 | Comparison between the oxidation states of niobium and iron before and after the photocatalytic reaction.** XPS spectra demonstrating a shift in binding energies of Nb 3d peaks (main fitted peaks in blue) between **a** Ni-Nb-MOF

before reaction, **b** Ni-Nb-MOF after reaction. XPS spectra demonstrating a shift in binding energies of Fe 2p peaks (main fitted peaks in green) between **c** Ni-Fe-MOF before reaction and **d** Ni-Fe-MOF after reaction.

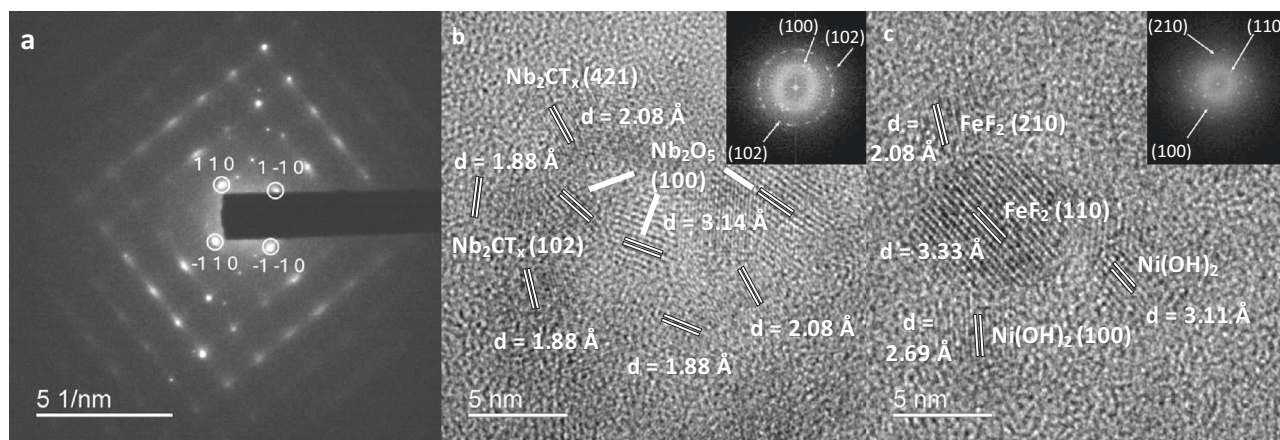


**Fig. 7 | Identification of in-situ formed species on the surface of Ni-Nb-MOF and Ni-Fe-MOF via HRTEM analysis.** **a** Selected Area Electron Diffraction (SAED) patterns of Ni-Nb-MOF after catalysis. HRTEM images and calculated d spacings of the

species formed on the surface of **b** Ni-Nb-MOF and **c** Ni-Fe-MOF after the photo-methanation reaction with their corresponding SAED insets.

and applications of MXenes-MOF composites are attracting increased research interest<sup>61,62</sup>, however, to our knowledge, this work is the first example of the in-situ formation of MXenes from a MOF backbone. Such structural reorganization is thought to occur within the induction time needed for the methane concentration to rise (75 mins). Similar observations were reported for CuO-Nb<sub>3</sub>O<sub>7</sub>(OH) hetero-nanostructure that remained inactive in the light-induced H<sub>2</sub> evolution reaction until it underwent an in-situ restructuring into Cu-Nb<sub>3</sub>O<sub>7</sub>(OH)<sup>63</sup>.

As for the active species that were derived from the Ni-Fe-MOF backbone, FFT calculations of the d spacings shown in Fig. 7c are in accordance with the (210) and (110) diffraction planes of FeF<sub>2</sub> with d spacings of 2.08 and 3.33 Å respectively<sup>64,65</sup>. Additionally, d spacings of 2.69 and 3.11 Å are attributed to Ni(OH)<sub>2</sub> particles with an inter-stratification of  $\alpha$  and  $\beta$  phases<sup>66</sup>. These species, formed upon MOF

degradation under the mild reaction conditions used, have oxidation states of (+II) for both Fe and Ni, which is also in accordance with the performed XPS results of the spent MOF and the binding energies reported in literature<sup>67,68</sup>. The N 1s peak, with a binding energy of 400 eV, is absent in the XPS spectrum of the spent Ni-Fe-MOF (Supplementary Figs. 38, 39), further confirming the absence of N among the active Ni and Fe species formed after the framework's destruction, which was attributed to the thermal loss of pyrazine as demonstrated by TGA-FTIR analysis (Supplementary Fig. 28). This hypothesis aligns well with the non-uniformity of the aggregates seen under AFM (Supplementary Fig. 18) and the decrease in organic content that can be concluded from ICP-OES (Supplementary Fig. 19b).

Similar structural alterations were reported in few MOF-based systems, one of which is NiMg-MOF-74 which selectively converted

CO<sub>2</sub> into methane when subjected to a thermal treatment at 350 °C that induced the reduction of Ni<sup>2+</sup> coordination sites into highly dispersed and active Ni<sup>0</sup> nanoclusters<sup>69</sup>.

## Discussion

Three isostructural MOFs, named NbOFFIVE-1-Ni, FeFFIVE-1-Ni, and AlFFIVE-1-Ni are tested as photo-methanation catalysts at mild conditions. While AlFFIVE-1-Ni was inactive, FeFFIVE-1-Ni did not withstand the conditions used, forming active but CO-selective species, hypothesized to be FeF<sub>2</sub> and Ni(OH)<sub>2</sub>, upon framework degradation. On the other hand, having demonstrated one of the highest CO<sub>2</sub> uptakes in confined spaces in previous reports, NbOFFIVE-1-Ni is, herein, reported to convert CO<sub>2</sub> to CH<sub>4</sub> with simultaneous high selectivity (~97%) and production rate (750 μmol<sup>g</sup><sub>catalyst</sub><sup>-1</sup>h<sup>-1</sup> at 180 °C) while retaining its crystallinity throughout the Sabatier process. This activity is attributed to the in-situ restructuring process, occurring during the reaction's induction time, in which Nb<sub>2</sub>CT<sub>x</sub>/Nb<sub>2</sub>O<sub>5</sub> nanoparticles active sites are proposed to form on the surface of the MOF backbone. Such MXenes/metal oxides heterojunctions are commonly known for their enhanced charge transfer effectiveness and photocatalytic potency, but are, as detailed in this work, pioneeringly derived from a MOF structure. Supporting evidence for this light-induced structural reorganization is obtained from the comparative characterization of the framework before and after catalysis. This structure-function interplay paves the way towards the design of active MOF-based catalysts for efficient the simultaneous CO<sub>2</sub> capture and solar fuel production.

## Methods

### Materials and chemicals

All chemicals used for the MOFs synthesis are commercially available and were used without further purification. Pyrazine (C<sub>4</sub>H<sub>4</sub>N<sub>2</sub>, ≥99%), nickel (II) nitrate hexahydrate (Ni(NO<sub>3</sub>)<sub>2</sub>·6H<sub>2</sub>O, laboratory reagent grade), niobium (V) oxide (Nb<sub>2</sub>O<sub>5</sub>, 99.99% trace metals basis), iron (III) nitrate nonahydrate (Fe(NO<sub>3</sub>)<sub>3</sub>·9H<sub>2</sub>O, laboratory reagent grade), aluminum nitrate nonahydrate (Al(NO<sub>3</sub>)<sub>3</sub>·9H<sub>2</sub>O, ≥98%) and hydrofluoric acid (HF, 48%) were purchased from Sigma Aldrich. Extreme care must be taken when handling HF, as it is highly toxic and corrosive.

### Synthesis of NbOFFIVE-1-Ni (Ni-Nb-MOF)

NbOFFIVE-1-Ni (Ni-Nb-MOF) was synthesized by dissolving pyrazine (4.80 mmol 384.40 mg), Ni(NO<sub>3</sub>)<sub>2</sub>·6H<sub>2</sub>O (0.60 mmol, 174.50 mg) and Nb<sub>2</sub>O<sub>5</sub> (0.60 mmol 79.70 mg) in 48% aqueous HF (7.15 mmol, 0.26 mL) in a 20 mL Teflon liner. Deionized water (3 mL) was added to dilute the mixture, and the autoclave was sealed and kept at 130 °C for 24 h. The reaction mixture was then left to cool to room temperature and the violet crystals were collected then washed with ethanol and left to air-dry. The obtained MOF powder was further activated at 105 °C under vacuum for 12 h.

### Synthesis of AlFFIVE-1-Ni (Ni-Al-MOF)

Pyrazine (4.80 mmol 384.40 mg), Ni(NO<sub>3</sub>)<sub>2</sub>·6H<sub>2</sub>O (0.60 mmol, 174.50 mg) and Al(NO<sub>3</sub>)<sub>3</sub>·9H<sub>2</sub>O (0.60 mmol, 225.0 mg) were dissolved in 0.26 mL of 48% aqueous HF, then diluted with 3 mL deionized water and placed in a 20 mL Teflon lined-autoclave heated at 85 °C for 24 h. After cooling, blue crystals were isolated, washed with ethanol, air-dried then activated at 105 °C under vacuum for 12 h.

### Synthesis of FeFFIVE-1-Ni (Ni-Fe-MOF)

Pyrazine (4.80 mmol 384.40 mg), Ni(NO<sub>3</sub>)<sub>2</sub>·6H<sub>2</sub>O (0.60 mmol, 174.50 mg) and Fe(NO<sub>3</sub>)<sub>3</sub>·9H<sub>2</sub>O (0.60 mmol, 232.3 mg) were dissolved in 0.26 mL of 48% aqueous HF, then diluted with 3 mL deionized water and placed in a 20 mL Teflon lined-autoclave heated at 85 °C for 24 h. After cooling, blue crystals were isolated, washed with ethanol, air-dried then activated at 105 °C under vacuum for 12 h.

## Characterization of the synthesized MOFs

The synthesized MOF crystals were characterized using X-ray diffractometer (Bruker D2-Phaser using Cu Kα radiation at 30 kV) and their morphologies were examined under Transmission Electron Microscopy (Hitachi HF-3300) and Scanning Electron Microscopy (MIRA3 Tescan). The thermal stability of each MOF candidate was assessed using Netzsch TG 209 F1 Libra TGA apparatus by heating ~10 mg of the MOF powder in a platinum crucible, under N<sub>2</sub> flow, from 30 to 1000 °C at a ramp rate of 10 °C/min. The optical properties of the three MOFs were determined using UV-vis diffuse reflectance spectroscopy (DRS) using a Lambda 1050 UV/vis/NIR PerkinElmer spectrometer with an integrating sphere. Cyclic voltammetry and electrochemical impedance spectroscopy measurements were performed in a three-electrode electrochemical workstation system (CHI 660e) with the FTO glass substrate (1 cm × 1 cm) as the working electrode, the Pt-wire as the auxiliary (counter) electrode and Ag/AgCl in saturated NaCl solution as the reference electrode. In brief, each sample (2 mg) was suspended in a 1 mL mixture of Nafion (100 μL, 0.5 wt%), water (450 μL), and ethanol (450 μL). The aqueous slurries were then drop-casted on the FTO electrode with 0.5 M Na<sub>2</sub>SO<sub>4</sub> solution used as a supporting electrolyte.

Atomic force microscopy (AFM) was performed on 60 μL of each solution drop cast on SiO<sub>2</sub> substrate (1 cm × 1 cm). The MOFs powders were dissolved in 2-Propanol (IPA) with a concentration of 1 mg/mL. The substrates were cleaned with three consecutive 15 min cycles in an ultrasonic bath using in order IPA, acetone, and IPA as cleaning solvents. The samples' topography was acquired with an NTEGRA II AFM from NT-MDT in ambient conditions (22 °C, relative humidity between 30 and 50%). The semi-contact (tapping) mode was used with an NSG10 cantilever (length 95 μm, width 30 μm, thickness 2 μm, resonant frequency 240 kHz, and force constant 11.8 N m<sup>-1</sup>).

Energy dispersive X-ray (EDX) analysis was performed using a FEI's Quanta 250 FEG ESEM with a variable 1–30 kV acceleration voltage, coupled to an EDAX silicon drift EDS detector with a 30 mm<sup>2</sup> window. X-ray photoelectron spectroscopy (XPS) results were extracted from Thermo Scientific Kα with an Al Kα X-ray source and were performed before and after the photo-methanation tests.

### Photo-methanation tests

The CO<sub>2</sub> photo-methanation tests were conducted similarly to our group's previous work<sup>70</sup>, in a flow-sealed Harrick high-temperature reactor equipped with a fused silica window at 180 °C under ambient pressure in a flow mode. First, 15 to 17 mg MOF catalyst (Ni-Nb-MOF, Ni-Al-MOF, and Ni-Fe-MOF respectively) was pressed and loaded into the reactor. Each sample was sealed into the reactor to which a fresh, continuous gas flow of CO<sub>2</sub> (3 sccm) and H<sub>2</sub> (3 sccm) was introduced for 900 min in each case. An OMEGA CN616A temperature controller equipped with a heating block was used to regulate the reaction's temperature. A LED source having a maximum intensity of 46 kW/m<sup>2</sup>, was used for irradiation, and its spectrum was recorded using an ASEQ LR1-B spectrometer. The source's current input was varied for intensity-dependent measurements. The generated products were quantified using an SRI-8610 gas chromatograph coupled to a flame ionization detector (FID) and equipped with 30 Mole Sieve 13a and 60 Haysep D columns. Control experiments were also conducted in the absence of CO<sub>2</sub> under the same conditions. Once Ni-Nb-MOF was identified as the most active and selective catalyst towards CH<sub>4</sub> formation, optimization tests were performed by changing the CO<sub>2</sub> to H<sub>2</sub> ratios (1:4), the reaction temperature [23: 240 °C]. It should be noted here that all photocatalytic tests were performed at least three times with an average error margin of 5%. To determine the amount of heat produced when the catalyst is exposed to light, a thermal imaging technique called infrared thermography was used. The catalyst bed's bulk temperature was measured using a forward-looking infrared

camera (FLIR) under different light intensities, similar to our previous report<sup>71</sup>. A Thermo-CAM EC320 FLIR thermal imaging camera was used to record the sample's temperature through the reactor's CaF<sub>2</sub> window while it was being illuminated with light. The MOF catalyst was positioned at the focal point of the LED light, ensuring it was placed at approximately the same distance from the light source as it is during operation within the reactor. The FLIR camera then measured the thermal radiation emitted from the light-exposed surface. <sup>13</sup>C isotope labeling tests were performed by purging needed ratios of <sup>13</sup>CO<sub>2</sub> and the gaseous products were analyzed using an Agilent 7890B-5977A MSD gas chromatography-mass spectrometer (GC-MS, via automated injection). The products were adequately separated and quantified through three capillary columns (Molsieve, HP-PLOT/Q + PT, and DB-FFAP) and the ratios of <sup>13</sup>C-labeled methane and carbon monoxide were calculated from the corresponding m/z. ~15–17 mg of each MOF sample was deposited on borosilicate filters for batch testing.

## Data availability

All data generated in this study are provided in the Supplementary Information/Source Data file. Source data are provided with this paper.

## References

- Jones, M. W. et al. National contributions to climate change due to historical emissions of carbon dioxide, methane, and nitrous oxide since 1850. *Sci. Data* **10**, 155 (2023).
- Ifandi, E. et al. Noble metal catalyst detection in rocks using machine-learning: The future to low-cost, green energy materials? *Sci. Rep.* **13**, 3765 (2023).
- Ohya, H. et al. Methanation of carbon dioxide by using membrane reactor integrated with water vapor permselective membrane and its analysis. *J. Membr. Sci.* **131**, 237–247 (1997).
- Kai, T., Yamasaki, Y., Takahashi, T., Masumoto, T. & Kimura, H. Increase in the thermal stability during the methanation of CO<sub>2</sub> over a Rh catalyst prepared from an amorphous alloy. *Can. J. Chem. Eng.* **76**, 331–335 (1998).
- Thampi, K. R., Kiwi, J. & Grätzel, M. Methanation and photo-methanation of carbon dioxide at room temperature and atmospheric pressure. *Nature* **327**, 506–508 (1987).
- Jelle, A. A. et al. Highly efficient ambient temperature CO<sub>2</sub> photo-methanation catalyzed by nanostructured RuO<sub>2</sub> on silicon photonic crystal support. *Adv. Energy Mater.* **8**, 1702277 (2018).
- O'Brien, P. G. et al. Photomethanation of gaseous CO<sub>2</sub> over Ru/silicon nanowire catalysts with visible and near-infrared photons. *Adv. Sci.* **1**, 1400001 (2014).
- Li, Y. et al. Photo-assisted CO/CO<sub>2</sub> methanation over Ni/TiO<sub>2</sub> catalyst: experiment and density functional theory calculation. *Chem-CatChem* **14**, e202200182 (2022).
- Rana, A. G., Ahmad, W., Al-Matar, A., Shawabkeh, R. & Aslam, Z. Synthesis and characterization of Cu-Zn/TiO<sub>2</sub> for the photocatalytic conversion of CO<sub>2</sub> to methane. *Environ. Technol.* **38**, 1085–1092 (2017).
- Adachi, K., Ohta, K. & Mizuno, T. Photocatalytic reduction of carbon dioxide to hydrocarbon using copper-loaded titanium dioxide. *Sol. Energy* **53**, 187–190 (1994).
- Mateo, D., Albero, J. & García, H. Titanium-perovskite-supported RuO<sub>2</sub> nanoparticles for photocatalytic CO<sub>2</sub> methanation. *Joule* **3**, 1949–1962 (2019).
- Lee, J. H. et al. Cost-effective and dynamic carbon dioxide conversion into methane using a CaTiO<sub>3</sub>@Ni-Pt catalyst in a photo-thermal hybrid system. *J. Photochem. Photobiol. A Chem.* **364**, 219–232 (2018).
- Hiragond, C. B., Powar, N. S., Kim, H. & In, S.-I. Unlocking solar energy: photocatalysts design for tuning the CO<sub>2</sub> conversion into high-value (C<sub>2</sub>+) solar fuels. *EnergyChem* **6**, 100130 (2024).
- Guo, K. et al. Boosting photocatalytic CO<sub>2</sub> reduction over a covalent organic framework decorated with ruthenium nanoparticles. *Chem. Eng. J.* **405**, 127011 (2021).
- Mateo, D., Albero, J. & García, H. Graphene supported NiO/Ni nanoparticles as efficient photocatalyst for gas phase CO<sub>2</sub> reduction with hydrogen. *Appl. Catal. B: Environ.* **224**, 563–571 (2018).
- Zhou, H. C., Long, J. R., & Yaghi, O. M. Introduction to metal-organic frameworks. *Chem. Rev.* **112**, 673–674 (2012).
- Ji, Z., Wang, H., Canossa, S., Wuttke, S. & Yaghi, O. M. Pore chemistry of metal-organic frameworks. *Adv. Funct. Mater.* **30**, 2000238 (2020).
- Furukawa, H., Cordova, K. E., O'Keeffe, M. & Yaghi, O. M. The chemistry and applications of metal-organic frameworks. *Science* **341**, 1230444 (2013).
- Ding, M., Flaig, R. W., Jiang, H.-L. & Yaghi, O. M. Carbon capture and conversion using metal-organic frameworks and MOF-based materials. *Chem. Soc. Rev.* **48**, 2783–2828 (2019).
- Trickett, C. A. et al. The chemistry of metal-organic frameworks for CO<sub>2</sub> capture, regeneration and conversion. *Nat. Rev. Mater.* **2**, 17045 (2017).
- Millward, A. R. & Yaghi, O. M. Metal-Organic Frameworks with Exceptionally High Capacity for Storage of Carbon Dioxide at Room Temperature. *J. Am. Chem. Soc.* **127**, 17998–17999 (2005).
- Llewellyn, P. L. et al. High uptakes of CO<sub>2</sub> and CH<sub>4</sub> in mesoporous metal-organic frameworks MIL-100 and MIL-101. *Langmuir* **24**, 7245–7250 (2008).
- Banerjee, R. et al. High-throughput synthesis of zeolitic imidazolate frameworks and application to CO<sub>2</sub> capture. *Science* **319**, 939–943 (2008).
- Lei, Z. et al. MOFs-based heterogeneous catalysts: new opportunities for energy-related CO<sub>2</sub> conversion. *Adv. Energy Mater.* **8**, 1801587 (2018).
- Lippi, R. et al. Highly active catalyst for CO<sub>2</sub> methanation derived from a metal organic framework template. *J. Mater. Chem. A* **5**, 12990–12997 (2017).
- Lin, X. et al. MOF-derived hierarchical hollow spheres composed of carbon-confined Ni nanoparticles for efficient CO<sub>2</sub> methanation. *Catal. Sci. Technol.* **9**, 731–738 (2019).
- Zhu, X. et al. Supercharged CO<sub>2</sub> photothermal catalytic methanation: High conversion, rate, and selectivity. *Angew. Chem.* **135**, e202218694 (2023).
- Mihet, M., Grad, O., Blanita, G., Radu, T. & Lazar, M. D. Effective encapsulation of Ni nanoparticles in metal-organic frameworks and their application for CO<sub>2</sub> methanation. *Int. J. Hydrog. Energy* **44**, 13383–13396 (2019).
- Cabrero-Antonino, M. et al. Design of cost-efficient and photocatalytically active Zn-based MOFs decorated with Cu<sub>2</sub>O nanoparticles for CO<sub>2</sub> methanation. *Chem. Commun.* **55**, 10932–10935 (2019).
- Wang, S. et al. A robust titanium isophthalate metal-organic framework for visible-light photocatalytic CO<sub>2</sub> methanation. *Chem* **6**, 3409–3427 (2020).
- Bhatt, P. M. et al. A fine-tuned fluorinated MOF addresses the needs for trace CO<sub>2</sub> removal and air capture using physisorption. *J. Am. Chem. Soc.* **138**, 9301–9307 (2016).
- Mukoyoshi, M. et al. Hybrid materials of Ni NP@MOF prepared by a simple synthetic method. *Chem. Commun.* **51**, 12463–12466 (2015).
- Cadiou, A. et al. Hydrolytically stable fluorinated metal-organic frameworks for energy-efficient dehydration. *Science* **356**, 731–735 (2017).
- Das, M., Nasani, R., Saha, M., Mobin, S. M. & Mukhopadhyay, S. Nickel(ii) complexes with a flexible piperazinyl moiety: studies on DNA and protein binding and catecholase like properties. *Dalton Trans.* **44**, 2299–2310 (2015).

35. Cabrero-Antonino, M., Ferrer, B., Baldoví, H. G. & Navalón, S. Toward solar-driven photocatalytic CO<sub>2</sub> methanation under continuous flow operation using benchmark MIL-125(Ti)-NH<sub>2</sub> supported ruthenium nanoparticles. *Chem. Eng. J.* **445**, 136426 (2022).
36. Khan, I. S. et al. An efficient metal-organic framework-derived nickel catalyst for the light driven methanation of CO<sub>2</sub>. *Angew. Chem.* **133**, 26680–26686 (2021).
37. Song, C. et al. Photothermal conversion of CO<sub>2</sub> with tunable selectivity using Fe-based catalysts: from oxide to carbide. *ACS Catal.* **10**, 10364–10374 (2020).
38. Dao, X.-Y. et al. Solvent-free photoreduction of CO<sub>2</sub> to CO catalyzed by Fe-MOFs with superior selectivity. *Inorg. Chem.* **58**, 8517–8524 (2019).
39. Li, X., Pramhaas, V., Rameshan, C., Blaha, P. & Rupprechter, G. Coverage-induced orientation change: CO on Ir(111) monitored by polarization-dependent sum frequency generation spectroscopy and density functional theory. *J. Phys. Chem. C. Nanomater Interfaces* **124**, 18102–18111 (2020).
40. Santos, J. L., Bobadilla, L. F., Centeno, M. A. & Odriozola, J. A. Operando DRIFTS-MS study of WGS and rWGS reaction on biochar-based Pt catalysts: the promotional effect of Na. *C* **4**, 47 (2018).
41. Gong, E. et al. Solar fuels: research and development strategies to accelerate photocatalytic CO<sub>2</sub> conversion into hydrocarbon fuels. *Energy Environ. Sci.* **15**, 880–937 (2022).
42. Zhao, J. et al. FeO-CeO<sub>2</sub> nanocomposites: an efficient and highly selective catalyst system for photothermal CO<sub>2</sub> reduction to CO. *NPG Asia Mater.* **12** (2020). <https://doi.org/10.1038/s41427-019-0171-5>
43. Zhang, Z. et al. Regulation the reaction intermediates in methanation reactions via modification of nickel catalysts with strong base. *Fuel* **237**, 566–579 (2019).
44. Bobadilla, L. F., Garcilaso, V., Centeno, M. & Odriozola, J. Monitoring the reaction mechanism in model biogas reforming by in situ transient and steady-state DRIFTS measurements. *ChemSusChem* **10** (2016). <https://doi.org/10.1002/cssc.201601379>
45. Li, L. et al. Research progress and reaction mechanism of CO<sub>2</sub> methanation over Ni-based catalysts at low temperature: a review. *Catalysts* **12**, 244 (2022).
46. Meng, N., Liu, C., Liu, Y., Yu, Y. & Zhang, B. Efficient electrosynthesis of syngas with tunable CO/H<sub>2</sub> ratios over ZnxCd1-xS-amine inorganic-organic hybrids. *Angew. Chem. Int. Ed.* **58**, 18908–18912 (2019).
47. Khan, S. et al. Recent advances on photo-thermo-catalysis for carbon dioxide methanation. *Int. J. Hydrog. Energy* **48**, 24756–24787 (2023).
48. Fan, W. K., Tahir, M. & Alias, H. Synergistic effect of nickel nanoparticles dispersed on MOF-derived defective Co<sub>3</sub>O<sub>4</sub> in situ grown over TiO<sub>2</sub> nanowires toward UV and visible light driven photothermal CO<sub>2</sub> methanation. *ACS Appl. Mater. Interfaces* **15**, 54353–54372 (2023).
49. Lemus-Santana, A. A., Rodríguez-Hernández, J., del Castillo, L. F., Basterrechea, M. & Reguera, E. Unique coordination of pyrazine in T[Ni(CN)<sub>4</sub>]<sub>2</sub>pyz with T=Mn, Zn, Cd. *J. Solid State Chem.* **182**, 757–766 (2009).
50. Lemus-Santana, A. A. et al. Synthesis and characterization of T[Ni(CN)<sub>4</sub>]<sub>2</sub>pyz with T=Fe, Ni; pyz=pyrazine: formation of T-pyz-Ni bridges. *J. Solid State Chem.* **184**, 2124–2130 (2011).
51. Pang, S.-Y., Io, W.-F., Wong, L.-W., Zhao, J. & Hao, J. Efficient energy conversion and storage based on robust fluoride-free self-assembled 1D niobium carbide in 3D nanowire network. *Adv. Sci.* **7**, 1903680 (2020).
52. Song, S. et al. Nb<sub>2</sub>O<sub>5</sub>/Nb<sub>2</sub>CT<sub>x</sub> composites with different morphologies through oxidation of Nb<sub>2</sub>CT<sub>x</sub> MXene for high-performance microwave absorption. *J. Alloy. Compd.* **843**, 155713 (2020).
53. Naguib, M. et al. Two-dimensional nanocrystals produced by exfoliation of Ti<sub>3</sub>AlC<sub>2</sub>. *Adv. Mater.* **23**, 4248–4253 (2011).
54. Naguib, M., Barsoum, M. W. & Gogotsi, Y. Ten years of progress in the synthesis and development of MXenes. *Adv. Mater.* **33**, 2103393 (2021).
55. Kuang, P., Low, J., Cheng, B., Yu, J. & Fan, J. MXene-based photocatalysts. *J. Mater. Sci. Technol.* **56**, 18–44 (2020).
56. Su, T. et al. One-step synthesis of Nb<sub>2</sub>O<sub>5</sub>/C/Nb<sub>2</sub>C (MXene) composites and their use as photocatalysts for hydrogen evolution. *ChemSusChem* **11**, 688–699 (2018).
57. Husmann, S. et al. Layered nano-mosaic of niobium disulfide heterostructures by direct sulfidation of niobium carbide MXenes for hydrogen evolution. *Adv. Mater. Interfaces* **9**, 2102185 (2022).
58. Manley, M. Near-infrared spectroscopy and hyperspectral imaging: non-destructive analysis of biological materials. *Chem. Soc. Rev.* **43**, 8200–8214 (2014).
59. Tonauer, C. M. et al. Near-infrared spectra of high-density crystalline H(2)O Ices II, IV, V, VI, IX, and XII. *J. Phys. Chem. A* **125**, 1062–1068 (2021).
60. Zhao, Y. et al. Photothermocatalytic sterilization activity enhancement and mechanism evaluation of WO<sub>3</sub>/TpPa-1/N-Nb<sub>2</sub>CT<sub>x</sub> constructed with a 2D Z-type heterojunction WO<sub>3</sub>/TpPa-1 and 2D cocatalyst Nb<sub>2</sub>CT<sub>x</sub>. *Ceram. Int.* **50**, 5336–5349 (2024).
61. Zhang, F. et al. Recent advances in MOFs/MXenes composites: synthesis and their electrochemical energy applications. *J. Energy Storage* **72**, 108213 (2023).
62. Safarkhani, M. et al. Engineering MXene@MOF composites for a wide range of applications: a perspective. *ACS Appl. Eng. Mater.* **1**, 3080–3098 (2023).
63. Hmadeh, M. et al. New hydrogen-evolution heteronanostructured photocatalysts: Pt-Nb<sub>3</sub>O<sub>7</sub>(OH) and Cu-Nb<sub>3</sub>O<sub>7</sub>(OH). *ChemSusChem* **7**, 2104–2109 (2014).
64. Zhang, S. et al. Novel FeF<sub>2</sub>/Fe<sub>1-x</sub>S nanoreactor-mediated mitochondrial dysfunction via oxidative stress and fluoride ions overloaded for synergistic chemodynamic therapy and photothermal therapy. *Adv. Funct. Mater.* **32**, 2113397 (2022).
65. Zhang, Y. et al. A novel sugar-assisted solvothermal method for FeF<sub>2</sub> nanomaterial and its application in LIBs. *Materials* **16**, 1437 (2023).
66. Fang, D.-L., Chen, Z.-D., Liu, X., Wu, Z.-F. & Zheng, C.-H. Homogeneous growth of nano-sized β-Ni(OH)<sub>2</sub> on reduced graphene oxide for high-performance supercapacitors. *Electrochim. Acta* **81**, 321–329 (2012).
67. Maulana, A. Y., Futralan, C. M. & Kim, J. MOF-derived FeF<sub>2</sub> nanoparticles@graphitic carbon undergoing in situ phase transformation to FeF<sub>3</sub> as a superior sodium-ion cathode material. *J. Alloy. Compd.* **840**, 155719 (2020).
68. Grosvenor, A. P., Biesinger, M. C., Smart, R. S. C. & McIntyre, N. S. New interpretations of XPS spectra of nickel metal and oxides. *Surf. Sci.* **600**, 1771–1779 (2006).
69. Zurrer, T. et al. Mixed-metal MOF-74 templated catalysts for efficient carbon dioxide capture and methanation. *Adv. Funct. Mater.* **31**, 2007624 (2021).
70. Xu, Y.-F. et al. Equilibrium photo-thermodynamics enables a sustainable methanol synthesis. *Joule* **7**, 738–752 (2023).
71. Tavasoli, A. et al. Enhanced hybrid photocatalytic dry reforming using a phosphated Ni-CeO<sub>2</sub> nanorod heterostructure. *Nat. Commun.* **14**, 1435 (2023).
72. Cabrero-Antonino, M. et al. Solar-driven gas phase photocatalytic CO<sub>2</sub> methanation by multimetallic UiO-66 solids decorated with RuOx nanoparticles. *Chem. Eng. J.* **468**, 143553 (2023).
73. Rueda-Navarro, C. M. et al. Solar gas-phase CO<sub>2</sub> hydrogenation by multifunctional UiO-66 photocatalysts. *ACS Catal.* **14**, 6470–6487 (2024).

## Acknowledgements

A.G. and G.O. ([www.solarfuels.utoronto.ca](http://www.solarfuels.utoronto.ca)) are grateful for the financial support of the Natural Sciences and Engineering Research Council of Canada (102723/14084) and Hydrofuel Canada Inc. K.H. and M.H. recognize the support of the K. Shair Central Research Science Laboratory and the University Research Board (URB) at the American University of Beirut. M.H. acknowledges the funding provided by the Arab Fund Fellowship Program. The authors acknowledge the Open Center for Characterization of Advanced Materials (OCCAM) facility for its support with TEM and Professor Clara Santato for her assistance with AFM.

## Author contributions

A.G., M.H., M.S., and G.O. ideated and supervised the study. A.G. and K.H. completed MOF synthesis and characterizations and carried out photocatalytic activity measurements. A.M. conducted DRIFTS experiments and analysis. C.M. performed the isotope labeling experiment. E.N. carried out the HRTEM, STEM, and SAED characterization, J.Y.H. supervised the HRTEM, STEM, and SAED characterization, J.Y. conducted the elemental analysis and A.C. performed AFM imaging and analysis. All authors contributed to writing the paper.

## Competing interests

The authors declare no competing interests.

## Additional information

**Supplementary information** The online version contains supplementary material available at <https://doi.org/10.1038/s41467-025-55891-1>.

**Correspondence** and requests for materials should be addressed to Abdelaziz Gouda, Mohini Sain, Mohamad Hmadeh or Geoffrey A. Ozin.

**Peer review information** *Nature Communications* thanks Yaguang Li, Su-Il In, and the other, anonymous, reviewers for their contribution to the peer review of this work. A peer review file is available.

**Reprints and permissions information** is available at <http://www.nature.com/reprints>

**Publisher's note** Springer Nature remains neutral with regard to jurisdictional claims in published maps and institutional affiliations.

**Open Access** This article is licensed under a Creative Commons Attribution-NonCommercial-NoDerivatives 4.0 International License, which permits any non-commercial use, sharing, distribution and reproduction in any medium or format, as long as you give appropriate credit to the original author(s) and the source, provide a link to the Creative Commons licence, and indicate if you modified the licensed material. You do not have permission under this licence to share adapted material derived from this article or parts of it. The images or other third party material in this article are included in the article's Creative Commons licence, unless indicated otherwise in a credit line to the material. If material is not included in the article's Creative Commons licence and your intended use is not permitted by statutory regulation or exceeds the permitted use, you will need to obtain permission directly from the copyright holder. To view a copy of this licence, visit <http://creativecommons.org/licenses/by-nc-nd/4.0/>.

© The Author(s) 2025